Highly Conducting Single-Molecule Topological Insulators Based on Mono- and Di-Radical Cations

Liang Li[⊥a], Jonathan Z. Low[⊥a], Jan Wilhelm[b], Guanming Liao[c], Suman Gunasekaran[a], Claudia R. Prindle[a], Rachel L. Starr[a], Dorothea Golze[d], Colin Nuckolls[a], Michael L. Steigerwald[a], Ferdinand Evers*[b], Luis M. Campos*[,a], Xiaodong Yin*[,c], Latha Venkataraman*[,a,e]

[⊥]equal contribution

[a]Department of Chemistry, Columbia University, New York, New York 10027, United States

[b]Institute of Theoretical Physics, University of Regensburg, Regensburg, Germany

[c]Beijing Key Laboratory of Photoelectronic/Electrophotonic Conversion Materials, School of Chemistry and Chemical Engineering, Beijing Institute of Technology, Beijing, 102488 P. R. China

[d]Technische Universität Dresden, König-Bau, Bergstrasse 66 c, 01069 Dresden, Germany

[e]Department of Applied Physics and Applied Mathematics, Columbia University, New York, New York 10027, United States

Abstract

Single-molecule topological insulators are promising candidates as conducting wires over nanometer length scales. In past, most conjugated molecular wires exhibit low conductance that decays as the wire length increases. To overcome this limitation, we studied a family of oligophenylene-bridged bis(triarylamines) with tunable and stable (mono-/di-)radicaloid character. The wires can undergo one- and two-electron chemical oxidations to the corresponding monocation and dication, respectively. We found that the oxidized wires exhibit high reversed conductance decay with increasing length, consistent with the expectation for the Su-Schrieffer-Heeger-type one-dimensional (1D) topological insulators. The champion 2.6 nm long dication displays a significantly high conductance greater than 0.1 G_0 ($2e^2/h$, the conductance quantum), 5400-fold greater than the neutral form. The observed conductance-length relationship is similar between monocation and dication series. DFT calculations elucidate how the frontier orbitals and delocalization of radicals facilitate the observed nonclassical quasi-metallic behavior. These findings offer new insights into molecular design of highly conducting 1D topological insulators.

Introduction

Designing long and highly conducting molecular wires has been a challenge from a theoretical and experimental perspective[1-4]. Most molecular wires studied as conductive elements of single-molecule circuits are designed using conjugated building blocks and typically conduct through a coherent and off-resonant mechanism. In this regime, conductance decreases exponentially with increasing length. One solution to this challenge is to create long conducting wires expressing minimal length-dependent conductance decay[5,6]. However, molecules with reverse conductance decay would be more desirable; that is, molecular wires with increasing conductance as their length increases[7]. This nonclassical trend has been proposed since the 1980s,[8,9] albeit most studies have been theoretical[10-12]. A commonly proposed method to achieve the anomalous inverse conductance-length relationship in such studies is to design molecular wires with diradicaloid character, following the Su-Schrieffer-Heeger (SSH) model for organic 1D topological insulators (so-called quasi-metallic polymers, eg. polyacetylene)[13-17]. Some of these concepts have been tested experimentally in single-molecule junctions by us and others using polymethines[18], cumulenes[19,20] and fused porphyrin oligomers[21]. However, electronic transmission through those molecules is far from the quantum of conductance ($G_0 = 2e^2/h$) that is expected within the SHH model.

In order to develop wires based on the SHH model, extended π-conjugation is necessary to afford highly conducting diradicaloid character, as well as stabilizing structural features that insulate the terminal radicals from the environment while maintaining strong coupling to the electrodes.[13,15,22] Considering that Thiele's and Chichibabin's hydrocarbons can be manipulated to display closed-shell and open-shell diradicaloid character (Figure 1A),[23] we posit that the more stable aza-derivatives can lead to the predicted behavior of 1D topological insulators. Motivated by the ability to chemically oxidize bis(triarylamines),[24] yielding stable mono- and di-radical cations, we designed and synthesized a series of oligophenylene bridged compounds (**B1-B4**, Figure 1A), with thioanisole functionality to bind to gold electrodes in a break-junction (see Methods and Supporting Information (SI) for details). As shown in Figure 1A, the doubly oxidized molecules exhibit quinoidal character bearing terminal radical cations on the nitrogen atoms, analogous to the polyacetylene wires described in the SSH model. Interestingly, we found that these systems exhibit remarkably high conductance, reminiscent of quasi-metallic wires.

The conductance of **B1-B4** single-molecule junctions was measured in their three different states: neutral (**Bn**), monocation ($\mathbf{Bn}^{+}$) and dication ($\mathbf{Bn}^{2+}$), with n = 1-4 *p*-phenylene bridging units. In the neutral state, conductance decreases exponentially with increasing length, in agreement with previous experimental and theoretical studies of coherent electron transport. In the singly and doubly oxidized forms however, conductance is remarkably high, and it increases with increasing length from n = 1 to 3, and then decreases slightly for n = 4. Notably, the conductance of $\mathbf{B3}^{+}$ and $\mathbf{B3}^{2+}$ is 1600 and 5400 times larger than the neutral

analogues, reaching a conductance greater than 0.1 G_0 for a 2.6 nm long molecule. From a theoretical analysis, this observed reversed conductance decay results from a strong delocalization of radicals among the frontier orbitals. The small decrease of conductance observed for **B4**$^{+}$ and **B4**$^{2+}$ indicates that this delocalization does not extend beyond three phenylene bridging units (1.4 nm)[25] as confirmed by DFT calculations. Our findings provide experimental insights into the behavior of 1D topological insulators that are not only based on diradical character, but also on systems with monoradical character – a property that has been overlooked in models of 1D topological insulators.[26]

Results and Discussion

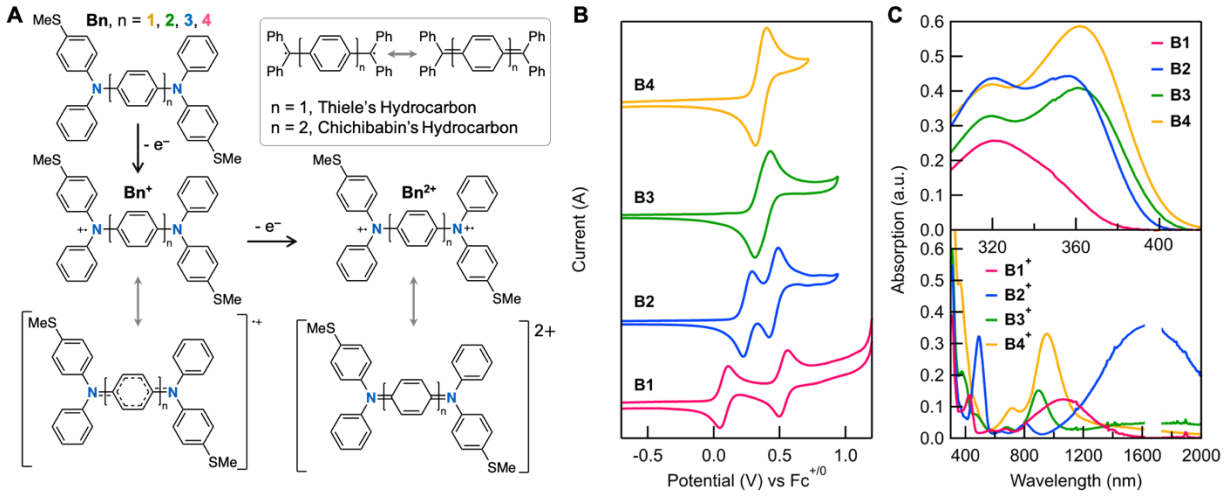

*Figure 1. (A) Chemical structures of the aza-derivatives of Thiele's and Chichibabin's hydrocarbons, in addition to their singly and doubly oxidized versions. (B) CVs showing the oxidation wave(s) of **B1-B4**. Oxidation potentials are given as $E_{1/2}$ values in the main text. (C) UV-Vis spectra of the **B1-B4** in their neutral (top panel) and monocation (bottom panel) states. The excised region in the bottom panel of (C) is where the detector switches, leading to a spike in the noise.*

We first characterize the spectroelectrochemical properties of **B1-B4** to determine their oxidation potentials, which are then used to select the appropriate chemical oxidant to generate the monocations and dications. The cyclic voltammograms (CVs) of **B1-B4** (Figure 1B) show stable and reversible oxidation waves at low positive potential, but no reduction waves are observed, even at a high reducing bias (up to -1.8 V vs Fc^{+}/Fc). Molecule **B1** shows two well-resolved oxidation peaks ($E_{1/2}$ = 0.08 V and 0.53 V). In **B2**, the onset of oxidation is at a higher potential, and the two distinct oxidation peaks ($E_{1/2}$ = 0.26 V and 0.45 V) appear closer together than in **B1**. In both cases, the two peaks correspond to two distinct one-electron oxidation waves at each nitrogen redox center. As the number of phenylene rings between the nitrogen atoms is increased, these two peaks coalesce into a broad peak for B3 and a single 2-electron oxidation peak for **B4** indicating that the nitrogen centers behave as independent redox entities in this longest wire.

Altogether, the CVs demonstrate that the coupling between the nitrogen centers decreases with increasing bridge length[27,28].

The steady-state absorption spectra of the neutral molecules in dichloromethane (Figure 1C) shows an onset between 410 nm (3.0 eV) and 380 nm (3.3 eV); molecules with such large optical gaps typically conduct through an off-resonant transport mechanism. Additionally, UV-Vis spectroscopy confirms the formation and stability in solution of the monocation and dication states upon chemical oxidation of the **Bn** molecules. To obtain solutions of the oxidized species, we use tris(4-bromophenyl)ammoniumyl hexachloroantimonate (BAHA) as a chemical oxidant, since its oxidizing potential of 0.7 V (vs Fc^+/Fc) is higher than those of **B1-B4**. Upon adding 1 equivalent (eq.) of BAHA, low energy absorption bands with peaks above 1000 nm (1.2 eV) appear in **B1-B3** as shown in Figure 1C (bottom panel, $\mathbf{B1}^+$: ~1000 nm; $\mathbf{B2}^+$: ~1600 nm; $\mathbf{B3}^+$: ~2000 nm). These very low-energy transitions are due to the intervalence charge transfer (IVCT) bands characteristic of mixed-valence states in bis(triarylamine) systems[27,28]. There is no IVCT absorption in **B4**, indicating a localized radical state. As one additional eq. of BAHA is added, there is a slight blue-shift with new bands appearing in the 800 –1200 nm region (see SI Figure S1), indicative of a transition from the open-shell semiquinoid monocation to the closed-shell quinoid dication.

We characterize the conductance of single-molecule junctions formed with **B1-B4** and their oxidized derivatives, using the scanning tunneling microscope-based break junction (STM-BJ) technique with Au electrodes[29,30] as detailed in the Methods section and the SI. Figure 2A shows the 1D conductance histograms for **B1-B3** in bromonaphthalene (BNP) measured at an applied bias of 50 mV (with a 97 kΩ resistor in series). All three histograms show clear conductance peaks, while **B4** shows a conductance signature only at applied biases above 500 mV (SI Figure S2). The peaks are broad due to the conductance plateaus being sloped, as the torsion angle between the thioanisole group and the conducting phenylene channel can change upon junction elongation[31]. This is most clearly seen in the two-dimensional (2D) conductance-displacement histograms (SI Figure S3). The 1D histograms of **B2** and **B3** show a single peak, while **B1** has a small shoulder at higher conductance, which we attribute to the conductance through the oxidized molecules (see below). The main peak in **B1** and the peaks in **B2-B4** are fit with a Gaussian to determine the peak conductance value, and these values are plotted against the number of phenylene units in the backbone (Figure 2D). An exponential decrease is seen with a decay constant β[**Bn**] = 1.7 per phenylene or 0.37 $Å^{-1}$ (SI Figure S4), consistent with other reported oligophenylene-based wires[30,32]. Considering that amines can also bind to gold to form junctions, this possibility was ruled out by STM-BJ measurements with an asymmetric control molecule (**mono-B2**$^+$), comprising only one thioanisole. This control does not exhibit any molecular conductance features, confirming that gold only binds to sulfur, and these tertiary amines are not capable forming a junction (SI Figure S5).

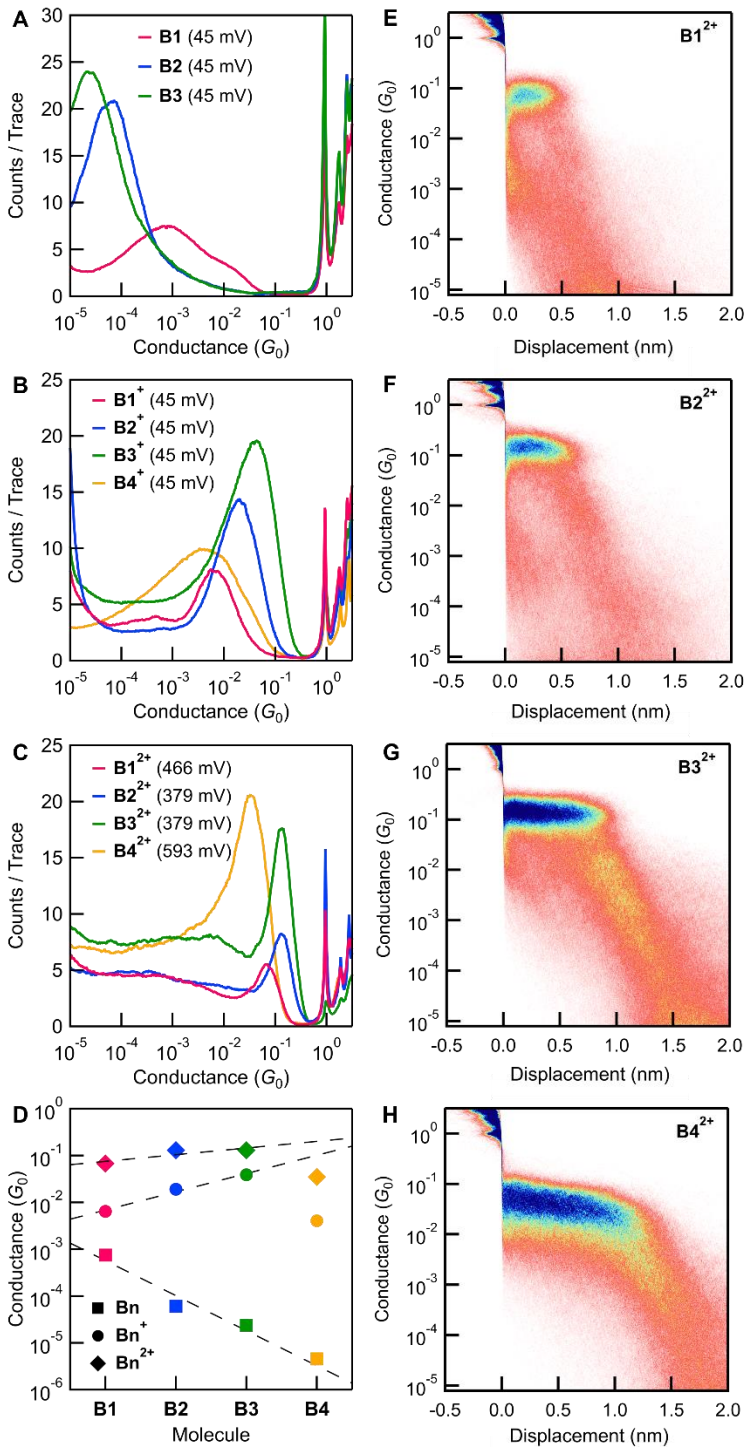

Figure 2. (A-C) Conductance histograms of the bis(triarylamine) wires in their (A) neutral state in BNP, and (B) monocation and (C) dication states in 1:3 DCM/BNP mixture. The applied bias is 50 mV for neutral and monocation series, and 750 mV for dication series. Average junction bias is indicated in parenthesis within the legends. (D) Conductance decay of the molecules with increasing length for all oxidation states. The β values are 1.7, -0.9, and -0.3 per phenyl for the neutral (squares), monocation (circles), and dication (diamond) series respectively. (E-H) 2D histograms of ***B1***$^{2+}$ *and* ***B4***$^{2+}$*, corresponding to (C).*

We next measure the conductance of the monocations generated by adding 1 eq. of BAHA to the solution of the neutral molecules. Since BAHA is only sparingly soluble in BNP, a 1:3 mixture of DCM and BNP was used as the solvent[33]. It is important to note that the histograms in Figure 2B show single conductance peaks, indicating that **B1**$^{+}$-**B4**$^{+}$ are stable, retaining their oxidation state in the junctions. However, the 1D histograms of **B1**$^{+}$-**B4**$^{+}$ (Figure 2B) show stark differences from those of **B1**-**B4** (Figure 2A and SI Figure S2). The conductance values of the monocation species are remarkably higher than those of their corresponding neutral species (see Figure S3 for 2D histograms). In particular, the conductance of **B3** changes from ~2.4×10^{-5} G_0 in the neutral state to ~ 3.9×10^{-2} G_0 in the monocation state (**B3**$^{+}$), a ~1600-fold increase. Furthermore, we note that 3.9×10^{-2} G_0 is an exceptionally high conductance for a molecule that has a long conductance pathway of ~2.6 nm, especially considering the low bias (45 mV) used in the measurements[32,34]. The increase in conductance results in a negative β[**Bn**$^{+}$] = −0.9 per phenylene (−0.21 Å^{-1}, see SI Figure S4). This trend is reliable, as measurements of **B1**$^{+}$-**B4**$^{+}$ in 1,2,4-trichlorobenzene also show an increase in conductance with length, albeit with β[**Bn**$^{+}$] = −0.4 per phenylene (SI Figure S6). This slightly different negative β is likely due to a solvent gating effect[35]. Interestingly, the longest molecule of the series, **B4**$^{+}$, shows a clear peak in the conductance histogram at 7.2×10^{-3} G_0 at a low bias, as opposed to its neutral counterpart. Although not as highly conductive as **B3**$^{+}$, the conductance value of **B4**$^{+}$ is still very large, and even higher than that of the neutral **B1**, the shortest molecule in the series. We also find that the histogram peak of **B4**$^{+}$ is much broader than those of the other monocations. This is consistent with structural information from DFT calculations (SI Figure S10), where we find that the dihedral angles between adjacent phenylenes increase from **B2**$^{+}$-**B4**$^{+}$. This observation correlates with the decrease of delocalization as the molecule gets longer, providing more structural flexibility in **B4**$^{+}$.[30]

To generate solutions of diradical cations **Bn**$^{2+}$, which are expected to have quinoidal resonance contributions, we mix 2 eq. of BAHA with **Bn** in a 1:3 mixture of DCM and BNP. At low biases, the conductance histograms are closer to those of the monocation indicating that the interaction with the electrodes reduce the dication to the monocation. Measurements at a higher applied bias (750 mV with a series resistor of 97 kΩ) yield conductance histograms with narrow peaks corresponding to junctions **B1**$^{2+}$-**B4**$^{2+}$. We note that both a high applied bias and the 2 eq. of BAHA are necessary to characterize the **Bn**$^{2+}$ series, as measurements of **B3** and **B4** at 750 mV and 600 mV bias respectively with 1 eq. and 2 eq. of BAHA give distinct conductance features from Figure 2C (SI Figure S7). This confirms that the high conductances seen in Figure 2C result from dication species, rather than resonant transport across the monocation at high biases or measurements in the same solutions without the molecule (SI Figure S8). Additionally, this also confirms that **B1**$^{2+}$-**B4**$^{2+}$ do not get reduced when bound to the electrodes at high biases. Figure 2E-2H show the 2D histograms for the measurements of **B1**$^{2+}$-**B4**$^{2+}$. The length of plateau increases with the molecular length. However, the plateaus for the dication series are shorter than the

monocation series which are slightly shorter than the neutral series. Past work has shown that both solvent and electrochemical potential affects plateau lengths[36,37]. Here, this suggests that the dication form can only be held in the junction for a certain threshold of tip-substrate distance, after which the junction breaks leaving a tail-like conductance feature indicative of through-space tunneling from the end of the molecule to the electrode. The narrow 1D histogram peaks and flat plateaus in 2D histograms of **B1**$^{2+}$-**B3**$^{2+}$ are also consistent with what would be expected from a near-coplanar structure of central phenylene chains, as evidenced by the DFT calculations in this oxidation state, which reveal a strong delocalization of the frontier orbitals[38] (see SI Figures S9 and S10). The slightly broader 1D peak and more tilted 2D plateau seen for **B4**$^{2+}$ indicates that the orbital delocalization is not sufficiently strong to prevent rotational flexibility unlike what we observe for **B1**$^{2+}$-**B3**$^{2+}$.

The key result from these measurements is that we find a negative β[**Bn**$^{2+}$] = −0.3 per phenylene (−0.07 Å^{-1}) for **B1**$^{2+}$-**B3**$^{2+}$ (Figure 2D) with junctions that are better conducting than the **B1**$^{+}$-**B4**$^{+}$ junctions, achieving a remarkably high conductance of 0.13 G_0 for **B3**$^{2+}$. For both oxidized series, beyond **B3**$^{+/2+}$ the conductance decreases, though it is still high considering the molecular length. The decrease in conductance of **B4**$^{+/2+}$ suggests that a decrease of coupling between the two nitrogen sites, reflected in the merged oxidation peaks from the CV data (Figure 1B). These wires thus form a unique molecular series that simultaneously exhibit ultra-high conductance at low biases over a 2.6 nm pathway and a negative conductance decay in both the semiquinoid and quinoid form. We note that a negative β for diradicaloid system is consistent with SHH model.[13,15] However, the observation of even larger negative β at a low applied bias for the monocation semiquinoid system is unique.

In order to relate the measured conductance to molecular structure, we calculate the transmission functions of molecular junctions formed with **B1-B4** using density functional theory (DFT) combined with non-equilibrium Green's function (NEGF) method using the FHI-aims package[39-41] (see Methods for details). We first relax the geometry of the isolated molecule with two Au atoms and then attach Au_{21} clusters that represent the electrodes as shown in Figure 3A for **B3**. The transmission functions for **B1-B4** are plotted against energy relative to Fermi energy (E_F) (Figure 3B), where the highest occupied molecular orbital (HOMO) and HOMO-1 resonances are indicated by solid and dashed arrows. From **B1** to **B4**, the HOMO resonance moves away from E_F while the HOMO-1 resonance moves towards E_F, decreasing the separation between the HOMO and HOMO-1 resonances with increasing molecular length. The transmission probability at E_F decreases exponentially with increasing number of phenylenes, yielding a β of 1.4 (Figure 3C), in good agreement with the experimental results for neutral series, despite known errors in DFT-based transmission calculations[42].

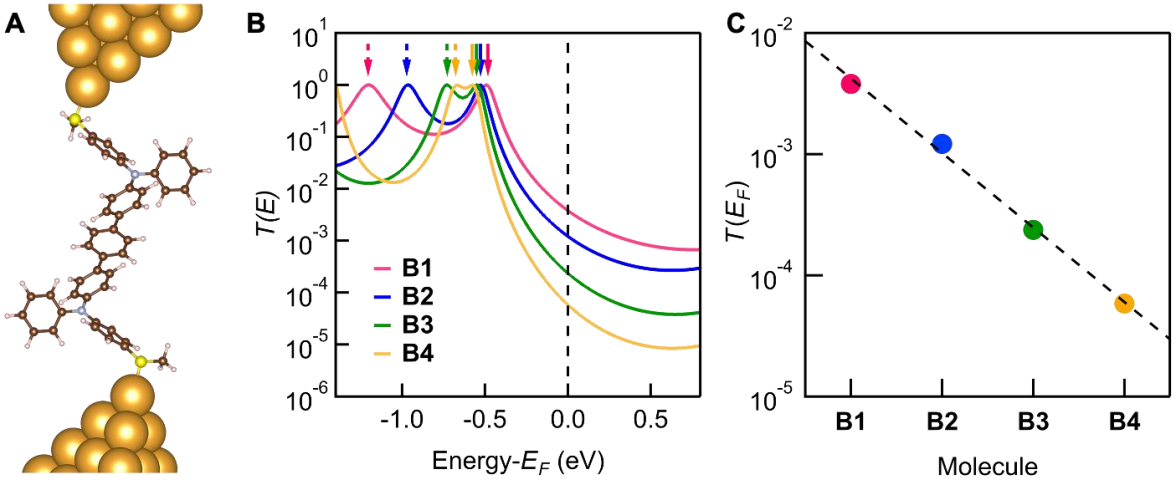

*Figure 3. (A) Relaxed structure of neutral **B3** bound to Au electrodes. Brown, light blue, yellow, light pink, and gold spheres represent C, N, S, H, and Au atoms, respectively. (B) Transmission functions of neutral **B1-B4**. E_F is indicated by the dashed line. The transmission resonances of HOMO and HOMO-1 orbitals are marked by solid arrows and dashed arrows, respectively. (C) Exponential decay of transmission at E_F, with $T(E_F) \sim e^{-\beta n}$ showing a decay constant β = 1.4 per phenylene.*

We now turn to transport calculations for the charged **B1**$^{+}$-**B4**$^{+}$ and **B1**$^{2+}$-**B4**$^{2+}$ series, which are more challenging for two reasons. First, the **B1**$^{+}$-**B4**$^{+}$ series constitute open-shell systems, which are notoriously difficult to describe with conventional DFT functionals[43]. Second, counter ions and the solvent in the experiment stabilize the charge on the molecule. They need to be included in an atomistic modeling, which can be done efficiently only by adopting a model situation that accounts for the delocalized nature of the compensating background charges. In the calculation (see Methods for details), we model the average counter charge by adding two square sheets of point charges above and below the molecule in the junction (Figure 4A and SI Figure S11). Charge neutrality of the positive molecule and counter charges is achieved by setting the total charge on the plates to be -1 and -2 for monocations and dications, respectively. To verify this arrangement of counter charges, we show in SI Table S2 that a DFT calculation indeed yields a positive excess charge mainly localized on the molecule rather than the electrodes. In addition, the SOMO orbital of **B4**$^{+}$ either in isolation or with electrodes and counter charges (Figure 4B) shares the same nodal structure within the polyphenylene chain with small discrepancies on the side groups. This illustrates that hybridization of the SOMO with the electrodes is rather weak, so that a weak-coupling picture of transport applies.

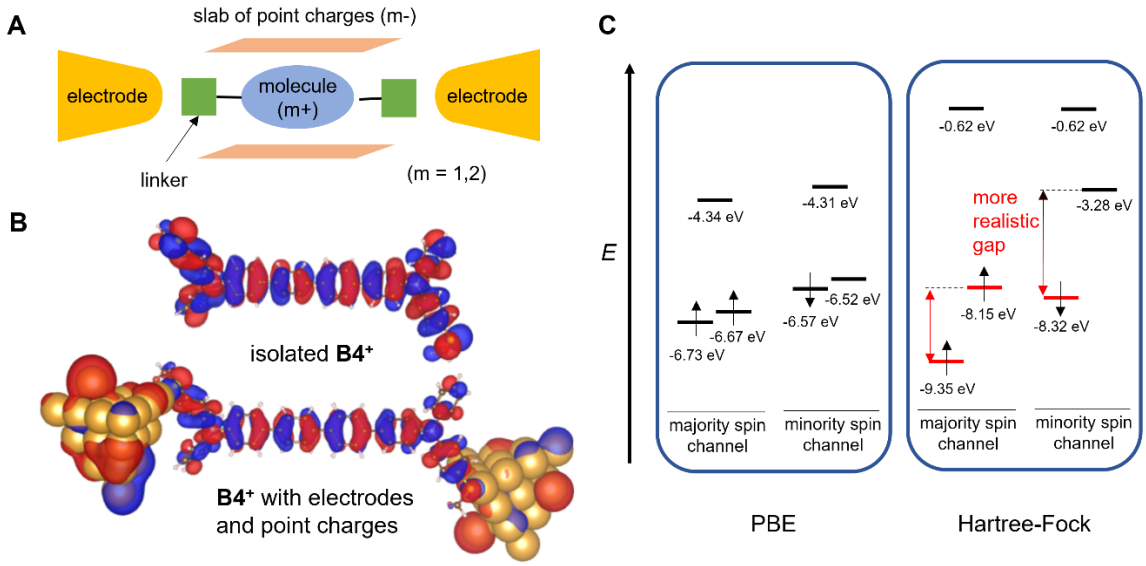

Figure 4. (A) Schematic of the DFT calculation model on monocation and dication series. (B) Comparison of the calculated SOMO orbital of an isolated ***B4***$^{+}$ *molecule, and* ***B4***$^{+}$ *in molecular junction with point charge. (C) Eigenvalues of frontier molecule orbitals of* ***B4***$^{+}$ *molecule, calculated by PBE and Hartree-Fock methods, respectively.*

For isolated monocations, we observe two frontier orbitals that are energetically nearly degenerate (Figure 4C). The near-degeneracy is an artifact of the PBE-functional used here which omits non-local exchange. When including non-local exchange via a Hartree-Fock calculation, the nearly degenerate levels split by about 1.2 eV and 5 eV in the majority and minority channels respectively (Figure 4C). As a result of this splitting the majority spin channel does not contribute significantly to the zero-bias conductance (SI Figure S13 and related discussion). We thus only include the spin-minority channel in our electron transport simulations of monocations. The resulting energy-resolved transmission function and corresponding zero-bias conductance, *G*, of the **Bn**$^{+}$ and **Bn**$^{2+}$ series is shown in Figure 5. With increasing length, the computational estimate for *G* exhibits a non-monotonous behavior with a maximum near **B3**$^{+/2+}$, in line with the experimental trend. The increase of conductance results from the energy gap shrinking between the two frontier resonances from **B1**$^{+}$ to **B3**$^{+}$ and from **B1**$^{2+}$ to **B3**$^{2+}$ (SI Figure S12A). Since the energy gap between these orbitals relates to the strength of coupling between the two radical states, with a larger gap indicating a stronger interaction[44,45], we can conclude that the coupling decreases as the wire length increases till **B3**$^{+/2+}$. For the longer wires, from **B3**$^{+}$ to **B4**$^{+}$ and **B3**$^{2+}$ to **B4**$^{2+}$, the gap remains nearly the same, while the coupling of frontier orbitals to the leads decreases resulting in narrower transmission resonances (SI Figure S12B) and lower zero-bias conductance.

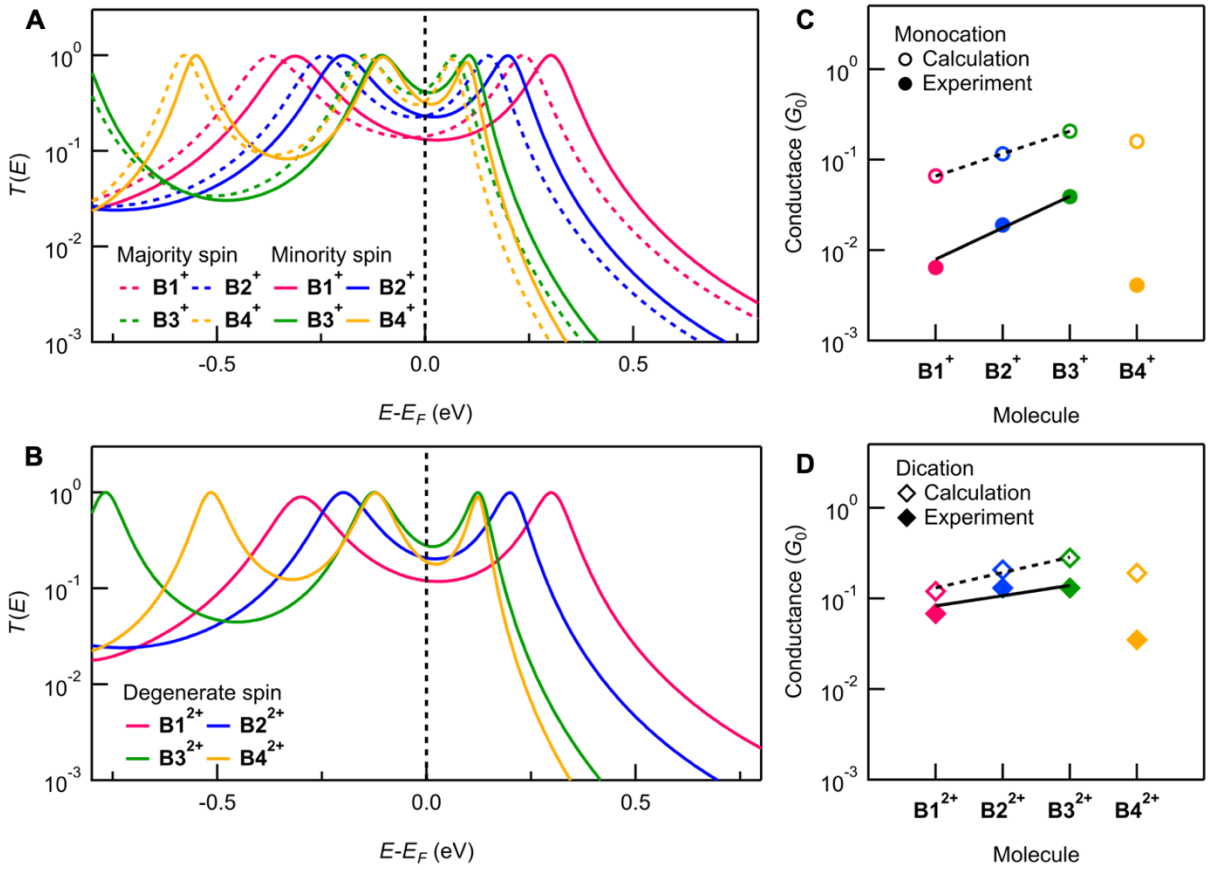

Figure 5. (A) Spin-polarized transmission for the monocation series. The majority spin channel and minority spin channel are marked as dashed lines and solid lines, respectively. (B) Closed-shell transmission calculation for the dication series. E_F is indicated by black dashed lines in (A) and (B). (C-D) Comparisons of calculated and measured conductance of the monocation and dication series, respectively. Both series show a reversed conductance decay from ***B1***$^{+/2+}$ *to* ***B3***$^{+/2+}$ *(calculated β values: -0.6 (monocation) and -0.4 (dication)) and a decrease in conductance for* ***B4***$^{+}$ *and* ***B4***$^{2+}$.

Finally, we relate the **Bn** series to the SSH model since the central chain of the doubly oxidized **Bn** and polyacetylene chain both show terminal diradical character. In polyacetylene chain, a reversed conductance decay is obtained at the short chain limit using tight-binding approach[18]. The wavefunction amplitude of each terminal radical is non-zero within the defined delocalization length (ξ). We find that if the chain length is shorter than ξ, the two radical states can have a significant overlap and couple to form the HOMO and LUMO states. When the chain grows longer, yet still shorter than ξ, the coupling is weakened decreasing the LUMO-HOMO gap (as shown in Figure 5B), leading to a reversed conductance decay as the diradical character increases significantly from **B1**$^{2+}$ to **B3**$^{2+}$ (SI Figure S14). This statement is supported by previous theoretical studies for cumulene[46] and polyphenylene[47] wires. If the chain is longer

than ξ, the two radical states will be decoupled, giving less and less electron density in the middle of the chain, and conductance will decrease with length. The long chain limit should be regarded as a typical 1D topological insulator since the terminal radical states themselves are still highly conducting (on edges but not through the entire chain), and the bulk states have much lower conductance. This behavior of 1D topological insulators at the 0D limit (short chain) is analogous to the cases of 3D topological insulators at the 2D limit (thin sheet), in which the top and bottom surface states will couple and open a gap, just like the HOMO and LUMO states generated from the two radical (edge) states. As the material gets thicker, the gap size will eventually be zero and the interior states become low conducting[48]. For the singly oxidized **Bn**, one should not regard them as the regular SSH-type 1D topological insulators since they don't show diradical characters on both edges. Similar to the dication series, the transmission functions of the monocations show a conductance-length dependence that is expected for an SSH-type 1D topological insulator. Therefore, we suggest that monocations could be an anomalous type of 1D topological insulators, in which the role of ξ would stay the same. For an infinitely long polyphenylene chain, the delocalization of a doped-radical state extends across 5 phenylenes[49]. In $\mathbf{Bn}^{+}$ and $\mathbf{Bn}^{2+}$ series, considering that the terminal nitrogens with lower on-site energy could trap the radicals and give a shorter ξ, it's reasonable that ξ is between 3 and 4 phenylenes, which leads to the conductance drop at $\mathbf{B4}^{+}$ and $\mathbf{B4}^{2+}$.

Acknowledgments. This work was supported in part by the NSF under grant DMR-1807580. J. Z. L. thanks the A*STAR Graduate Academy in Singapore for a graduate fellowship. S.G was supported by a NSF Graduate Research Fellowship under grant DGE-1644869. C.R.P. was supported by a National Defense Science and Engineering Graduate Fellowship. X.Y. and G.L. acknowledge to Analysis and Testing center of Beijing Institute of Technology for characterization in NMR and HR-MS. X.Y. acknowledge to Beijing Institute of Technology Research Fund Program for Young Scholars. G. L. thanks the Project of the Science Funds of Jiangxi Education Office (GJJ180629) and the Project of Jiangxi Science and Technology Normal University (2016XJZD009) for financial support. J. W. and F. E. thank M. Camarasa-Gomez for helpful discussions. J. W. and F. E. acknowledge the Gauss Centre for Supercomputing for providing computational resources on SuperMUC-NG at the Leibniz Supercomputing Centre under the Project ID pn72pa. The work in Regensburg has been supported by the Deutsche Forschungsgemeinschaft (DFG, German Research Foundation) through Project ID 314695032 (SFB 1277, subprojects A03 and B01).

Author Contributions. L.L and J.Z.L performed all STM measurements. J. W. and L.L. performed all DFT calculations. G.L., R.L.S., C.R.P. and X.Y. performed all the synthesis. L.L., J.Z.L, J. W., X.Y., F. E., L.M.C and L.V. wrote the paper with contributions from all authors. L.V., X.Y., F. E. and L.M.C. oversaw the project.

Competing financial interests. Authors declare no competing financial interests.

Data availability. The data that support the findings of this study not included in the supplementary information document are available from the corresponding author upon reasonable request.

Code Availability Statement. The data that support the findings was acquired using a custom instrument controlled by custom software (Igor Pro, Wavemetrics). The software is available from the corresponding author upon reasonable request.

Materials & Correspondence Reprints and permissions information is available online. Readers are welcome to comment on the online version of the paper. Correspondence and requests for materials should be addressed to L.V.: lv2117@columbia.edu, F.E.: Ferdinand.evers@physik.uni-regensberg.de. X.Y.: yinxd18@bit.edu.cn and L.M.C.: lcampos@columbia.edu.

Methods

Synthesis: All reactions and manipulations were carried out under an atmosphere of pre-purified nitrogen or argon using Schlenk techniques. All solvents used for experiments were purified using a solvent purification system. All reagents used in the synthesis were purchased from Sigma-Aldrich, and directly used without purification. 4-(methylthio)-N-phenylaniline was prepared according to literature[50].

^{1}H-NMR were recorded on a Bruker Avance III 400 (400 MHz) and ^{13}C-NMR were recorded on a Bruker Avance III 500 (500 MHz) spectrometer, in Acetone-d6 (residual solvent peak at $\delta = 2.05$ ppm for ^{1}H-NMR, and at $\delta = 29.84, 206.13$ ppm for ^{13}C-NMR).

Mass spectra were obtained at the Columbia University mass spectrometry facility using a XEVO G2-XS Waters® equipped with a QTOF detector with multiple inlet and ionization capabilities including electrospray ionization (ESI), atmospheric pressure chemical ionization (APCI), and atmospheric solids analysis probe (ASAP). The base peaks were usually obtained as $[M]^+$ or $[M+H]^+$ ions.

Spectroscopy: UV-visible absorption data were acquired on a Varian Cary 5000 UV-Vis/NIR spectrophotometer. Cyclic voltammograms (CVs) were recorded on a CHI 66 electrochemical workstation using Pt plate electrode as working electrode, Pt wire as counter electrode, and Ag/AgCl electrode as the reference electrode at room temperature.

Conductance Measurements: STM-BJ conductance measurements were done using a custom-built modified Scanning Tunneling Microscope (STM)[30]. We used 0.25 mm diameter cut gold wire (99.95%, Alfa Aesar) as the STM tip and ~100 nm gold-coated (99.999%, Alfa Aesar) steel pucks as substrates. A commercially available single-axis piezoelectric positioner (P-840.10, PI) was used to achieve sub-angstrom level control of the tip-substrate distance. The STM was controlled using a custom software written in IgorPro (Wavemetrics, Inc.) and operated under ambient conditions at room temperature. The gold substrates were

UV/ozone cleaned for 20 minutes prior to use. For each measurement, 1000 traces were first collected prior to adding molecular solutions to check the cleanliness of the gold surface. Solutions of the target molecules at 20 μM concentration were added to the substrate for STM break-junction measurements. The solvents for the solutions are bromonaphthalene (BNP) for **B1**-**B4**, and dichloromethane (DCM)/bromonaphthalene (BNP) in a ratio of 1:3 for $\mathbf{B1}^{+}$-$\mathbf{B4}^{+}$ and $\mathbf{B1}^{2+}$-$\mathbf{B4}^{2+}$. After the formation of each Au-Au junction with a conductance greater than 5 G_0, the piezoelectric positioner moved the tip at a speed of 20 nm/s to break the junction. The current and voltage across the junction were measured at 40 kHz with a voltage applied across the junction in series with a 97 kΩ resistor. The junction voltage is therefore always smaller than the applied voltage and depends on the junction conductance as indicated in the figures. During the retraction, a gold point-contact is formed with a conductance close to 1 G_0. When this contact is broken in a solution of molecules terminated with gold binding groups, such as the thioanisole groups used here, molecular conductance plateaus are observed below 1 G_0. The measured conductance (current/voltage) traces were then collected and compiled into logarithmically binned 1D conductance histograms, while 2D conductance-displacement histograms were obtained by overlaying all the measured traces after aligning them at a conductance of 0.5 G_0. 3000 traces are measured for the neutral and monocation series, and 4000 traces are measured for the dication series without data selection. The traces are acquired consecutively and analyzed without data selection.

DFT Methods: DFT calculations were carried out using closed-shell Kohn-Sham formulation of density functional theory with FHI-aims software[39]. A non-empirical generalized gradient-corrected approximation (PBE) for the exchange-correlation functional[51] was used. Scalar relativistic corrections to the kinetic energy were incorporated in the first-principles calculations at the atomic zeroth-order regular approximation (ZORA) level[52]. The Kohn-Sham states were represented in an optimized all-electron numeric atom-centered basis set with "tight" computational settings (roughly equivalent to "double zeta + polarization" quality for the molecular atoms and "double zeta" quality for the gold atom which belong to the electrodes in transmission calculations). The calculation results were obtained using standard convergence criteria in the self-consistent field cycle for the difference in the particle density (10^{-5} electrons/Å^3), total energy (10^{-6} eV), sum of Kohn-Sham eigenvalues (10^{-4} eV) and forces (10^{-4} eV/Å). In the calculations of the charged molecules attached to the electrodes, we use point charges arranged on two parallel squares above and below the central molecule with inter-sheet distance of 10 Å, consisting of 15×15 evenly distributed point charges. For $\mathbf{B1}^{+}$ and $\mathbf{B1}^{2+}$, the edge length of the square sheets is 8 Å. Otherwise, the edge length is 12 Å (SI Figure S11). The energy-dependent transmission functions were calculated using the non-equilibrium Green's function formalism with the transport package AITRANSS[40,41,53]. The junction electrodes were modeled by tetrahedral clusters of 22 atoms each with interatomic distance of 2.88 Å. The self-energy of the electron reservoirs was constructed by a Markovian

spatially local function ($\Sigma(\mathbf{r}, \mathbf{r}') = i\eta(\mathbf{r})\delta(\mathbf{r} - \mathbf{r}')$). The local absorption rate $\eta(\mathbf{r})$ was adjusted to guarantee that smooth change in $\eta(\mathbf{r})$ doesn't affect the electronic transmission. The Fermi level for transport calculations on charged molecules is set in the middle between transmission peaks associated with SOMO and LUMO (for monocations) and HOMO and LUMO (for dications). The resulting trends of the zero-bias conductance with increasing wire length is identical over a major energy window and does not depend on the exact location of the Fermi level. For the Hartree-Fock calculation on the gas-phase $\mathbf{B4}^+$, we have used the dscf program of the TURBOMOLE package and a def2-TZVP basis set[54].

REFERENCES

1. Davis, W. B., Svec, W. A., Ratner, M. A. & Wasielewski, M. R. Molecular-wire behaviour in p-phenylenevinylene oligomers. *Nature* **396**, 60-63 (1998).
2. Nitzan, A. & Ratner, M. A. Electron transport in molecular wire junctions. *Science* **300**, 1384-1389 (2003).
3. Choi, S. H., Kim, B. & Frisbie, C. D. Electrical resistance of long conjugated molecular wires. *Science* **320**, 1482-1486 (2008).
4. Lafferentz, L. et al. Conductance of a Single Conjugated Polymer as a Continuous Function of Its Length. *Science* **323**, 1193-1197 (2009).
5. Sedghi, G. et al. Long-range electron tunnelling in oligo-porphyrin molecular wires. *Nature nanotechnology* **6**, 517-523 (2011).
6. Nacci, C. et al. Conductance of a single flexible molecular wire composed of alternating donor and acceptor units. *Nature communications* **6**, 1-8 (2015).
7. Zhou, Y. et al. Quantum length dependence of conductance in oligomers: First-principles calculations. *Physical Review B* **75**, 245407 (2007).
8. Reimers, J. & Hush, N. Electron transfer and energy transfer through bridged systems. I. Formalism. *Chemical Physics* **134**, 323-354 (1989).
9. Joachim, C. Ligand-length dependence of the intramolecular electron transfer through-bond coupling parameter. *Chemical physics* **116**, 339-349 (1987).
10. Tsuji, Y., Movassagh, R., Datta, S. & Hoffmann, R. Exponential attenuation of through-bond transmission in a polyene: Theory and potential realizations. *ACS nano* **9**, 11109-11120 (2015).
11. Li, S., Gan, C. K., Son, Y.-W., Feng, Y. P. & Quek, S. Y. Anomalous length-independent frontier resonant transmission peaks in armchair graphene nanoribbon molecular wires. *Carbon* **76**, 285-291 (2014).

12. Gil-Guerrero, S., Peña-Gallego, Á., Ramos-Berdullas, N., Martin Pendas, A. & Mandado, M. Assessing the reversed exponential decay of the electrical conductance in molecular wires: the undeniable effect of static electron correlation. *Nano letters* **19**, 7394-7399 (2019).
13. Heeger, A. J., Kivelson, S., Schrieffer, J. & Su, W.-P. Solitons in conducting polymers. *Reviews of Modern Physics* **60**, 781 (1988).
14. Cirera, B. et al. Tailoring topological order and π-conjugation to engineer quasi-metallic polymers. *Nature nanotechnology* **15**, 437-443 (2020).
15. Su, W. P., Schrieffer, J. & Heeger, A. J. Solitons in polyacetylene. *Physical review letters* **42**, 1698 (1979).
16. Stuyver, T., Zeng, T., Tsuji, Y., Geerlings, P. & De Proft, F. Diradical character as a guiding principle for the insightful design of molecular nanowires with an increasing conductance with length. *Nano letters* **18**, 7298-7304 (2018).
17. Hernangómez-Pérez, D., Gunasekaran, S., Venkataraman, L. & Evers, F. Solitonics with polyacetylenes. *Nano letters* **20**, 2615-2619 (2020).
18. Gunasekaran, S. et al. Near length-independent conductance in polymethine molecular wires. *Nano letters* **18**, 6387-6391 (2018).
19. Zang, Y. et al. Cumulene Wires Display Increasing Conductance with Increasing Length. *Nano Letters* **20**, 8415-8419 (2020).
20. Xu, W. et al. Unusual Length Dependence of the Conductance in Cumulene Molecular Wires. *Angewandte Chemie International Edition* **58**, 8378-8382 (2019).
21. Leary, E. et al. Bias-driven conductance increase with length in porphyrin tapes. *Journal of the American Chemical Society* **140**, 12877-12883 (2018).
22. Meier, E. J., An, F. A. & Gadway, B. Observation of the topological soliton state in the Su–Schrieffer–Heeger model. *Nature communications* **7**, 1-6 (2016).
23. Montgomery, L. K., Huffman, J. C., Jurczak, E. A. & Grendze, M. P. The molecular structures of Thiele's and Chichibabin's hydrocarbons. *Journal of the American Chemical Society* **108**, 6004-6011 (1986).
24. Su, Y. et al. Tuning Ground States of Bis (triarylamine) Dications: From a Closed-Shell Singlet to a Diradicaloid with an Excited Triplet State. *Angewandte Chemie* **126**, 2901-2905 (2014).
25. Heeger, A. J. Semiconducting and metallic polymers: the fourth generation of polymeric materials (Nobel lecture). *Angewandte Chemie International Edition* **40**, 2591-2611 (2001).
26. Joubert-Doriol, L. & Izmaylov, A. F. Molecular "topological insulators": a case study of electron transfer in the bis(methylene) adamantyl carbocation. *Chemical Communications* **53**, 7365-7368 (2017).

27. Lambert, C. & Nöll, G. The class II/III transition in triarylamine redox systems. *Journal of the American Chemical Society* **121**, 8434-8442 (1999).
28. Low, P. J. et al. Crystal, Molecular and Electronic Structure of N, N′-Diphenyl-N, N′-bis (2, 4-dimethylphenyl)-(1, 1′-biphenyl)-4, 4′-diamine and the Corresponding Radical Cation. *Chemistry–A European Journal* **10**, 83-91 (2004).
29. Xu, B. & Tao, N. J. Measurement of single-molecule resistance by repeated formation of molecular junctions. *science* **301**, 1221-1223 (2003).
30. Venkataraman, L. et al. Single-Molecule Circuits with Well-Defined Molecular Conductance. *Nano Letters* **6**, 458 - 462 (2006).
31. Park, Y. S. et al. Frustrated rotations in single-molecule junctions. *Journal of the American Chemical Society* **131**, 10820-10821 (2009).
32. Zang, Y. et al. Electronically transparent Au–N bonds for molecular junctions. *Journal of the American Chemical Society* **139**, 14845-14848 (2017).
33. Low, J. Z. et al. The Environment-Dependent Behavior of the Blatter Radical at the Metal–Molecule Interface. *Nano Letters* **19**, 2543-2548 (2019).
34. Lu, Q. et al. From tunneling to hopping: a comprehensive investigation of charge transport mechanism in molecular junctions based on oligo (p-phenylene ethynylene) s. *ACS Nano* **3**, 3861-3868 (2009).
35. Fatemi, V., Kamenetska, M., Neaton, J. & Venkataraman, L. Environmental control of single-molecule junction transport. *Nano letters* **11**, 1988-1992 (2011).
36. Choi, B. et al. Solvent-dependent conductance decay constants in single cluster junctions. *Chemical science* **7**, 2701-2705 (2016).
37. Capozzi, B. et al. Tunable charge transport in single-molecule junctions via electrolytic gating. *Nano letters* **14**, 1400-1404 (2014).
38. Delaney, P., Nolan, M. & Greer, J. Symmetry, delocalization, and molecular conductance. *The Journal of chemical physics* **122**, 044710 (2005).
39. Blum, V. et al. Ab initio molecular simulations with numeric atom-centered orbitals. *Computer Physics Communications* **180**, 2175-2196 (2009).
40. Arnold, A., Weigend, F. & Evers, F. Quantum chemistry calculations for molecules coupled to reservoirs: formalism, implementation, and application to benzenedithiol. *The Journal of chemical physics* **126**, 174101 (2007).
41. Bagrets, A. Spin-polarized electron transport across metal–organic molecules: a density functional theory approach. *Journal of chemical theory and computation* **9**, 2801-2815 (2013).

42. Quek, S. Y. et al. Amine− gold linked single-molecule circuits: experiment and theory. *Nano Letters* **7**, 3477-3482 (2007).
43. Evers, F., Korytár, R., Tewari, S. & van Ruitenbeek, J. M. Advances and challenges in single-molecule electron transport. *Reviews of Modern Physics* **92**, 035001 (2020).
44. Klausen, R. S. et al. Evaluating atomic components in fluorene wires. *Chemical Science* **5**, 1561-1564 (2014).
45. Yoshizawa, K. An orbital rule for electron transport in molecules. *Accounts of chemical research* **45**, 1612-1621 (2012).
46. Garner, M. H., Bro-Jørgensen, W., Pedersen, P. D. & Solomon, G. C. Reverse bond-length alternation in cumulenes: candidates for increasing electronic transmission with length. *The Journal of Physical Chemistry C* **122**, 26777-26789 (2018).
47. Gil-Guerrero, S., Ramos-Berdullas, N., Pendás, Á. M., Francisco, E. & Mandado, M. Anti-ohmic single molecule electron transport: is it feasible? *Nanoscale Advances* **1**, 1901-1913 (2019).
48. Asmar, M. M., Sheehy, D. E. & Vekhter, I. Topological phases of topological-insulator thin films. *Physical Review B* **97**, 075419 (2018).
49. Brédas, J.-L., Chance, R. & Silbey, R. Comparative theoretical study of the doping of conjugated polymers: polarons in polyacetylene and polyparaphenylene. *Physical Review B* **26**, 5843 (1982).
50. Madrid, P. B., Polgar, W. E., Toll, L. & Tanga, M. J. Synthesis and antitubercular activity of phenothiazines with reduced binding to dopamine and serotonin receptors. *Bioorganic & medicinal chemistry letters* **17**, 3014-3017 (2007).
51. Perdew, J. P., Burke, K. & Ernzerhof, M. Generalized gradient approximation made simple. *Physical review letters* **77**, 3865 (1996).
52. Lenthe, E. v., Baerends, E.-J. & Snijders, J. G. Relativistic regular two-component Hamiltonians. *The Journal of chemical physics* **99**, 4597-4610 (1993).
53. Wilhelm, J., Walz, M., Stendel, M., Bagrets, A. & Evers, F. Ab initio simulations of scanning-tunneling-microscope images with embedding techniques and application to C 58-dimers on Au (111). *Physical Chemistry Chemical Physics* **15**, 6684-6690 (2013).
54. Balasubramani, S. G. et al. TURBOMOLE: Modular program suite for ab initio quantum-chemical and condensed-matter simulations. *The Journal of chemical physics* **152**, 184107 (2020).